Experiments in Fluids (2023) 64:179
https://doi.org/10.1007/s00348-023-03718-4

RESEARCH ARTICLE

Experimental investigation of heating augmentation by particle kinetic energy conversion in dust-laden supersonic flows

Dirk Allofs[1] · **Dominik Neeb**[1] · **Ali Gülhan**[1]

Received: 4 April 2023 / Revised: 25 September 2023 / Accepted: 28 September 2023 / Published online: 30 October 2023

Abstract

The presence of particles in supersonic flows can cause significant increases in stagnation point heat fluxes (Dunbar et al. in AIAA J 13:908–912, 1975). This effect is commonly named 'particle-induced heat flux augmentation' or just 'heating augmentation.' Heating augmentation can be described as the sum of the conversion of kinetic energy of the particles into thermal energy, characterized by the energy conversion efficiency, also called accommodation coefficient, and the increase of convective heat flux (Polezhaev et al. in High Temp 30:1147–1153, 1992; Vasilevskii and Osiptsov in Experimental and numerical study of heat transfer on a blunt body in dusty hypersonic flow 33rd thermophysics conference, American Institute of Aeronautics and Astronautics, 1999). Although the accommodation coefficient is fundamental for heating augmentation characterization, there is only a small number of experimental datasets for it. This work focusses on the experimental determination of the accommodation coefficient in flow regimes at Mach number 2.1, Reynolds number, based on the probe nose diameter, from approx. 6e5 to 1.8e6, and nominal particle sizes of approx. 20 µm. The decrease of particle velocity and kinetic energy flux in the shock layer is measured with highly resolved shadowgraphy for individual particles. The particle kinetic energy flux is decreased by 29% on average by particle deceleration in the shock layer. Negligible kinetic energy fluxes of rebounded particles were measured. The accommodation coefficient is approx. 0.36 for Al_2O_3 and SiO_2 particles, while it is approx. 0.09 for MgO particles. Hence, it is significantly smaller than the widely used value of 0.7, based on the study of (Fleener and Watson in Convective heating in dust-laden hypersonic flows 8th thermophysics conference, 1973), but in good agreement with values given in (Hove and Shih in Reentry vehicle stagnation region heat transfer in particle environments 15th aerospace sciences meeting, 1977) and (Molleson and Stasenko in High Temp 55:87–94, 2017. https://doi.org/10.1134/S0018151X1701014X). No difference between erosive and elastic particle reflection mode was detected on the conversion efficiency. The data from a simplification of the modeling approach of the conversion efficiency for elastic particle reflection by Molleson and Stasenko (2017) are in poor agreement with experimental data.

List of symbols

$\dot{e}_{\text{kin reb}}$	Kinetic energy flux of rebounded particles (kW/m^2)
$\dot{e}_{\text{kin inc}}$	Kinetic energy flux of incident particles (kW/m^2)
$\dot{q}_0$	Stagnation point heat flux in a dust-free flow (kW/m^2)
$\dot{q}_a$	Direct energy transfer from particles into the probe (kW/m^2)
$\dot{q}_{SP}$	Stagnation point heat flux (kW/m^2)
$\dot{q}_\Sigma$	Stagnation point heat flux in a dust-laden flow (kW/m^2)
a_{heat}	Thermal energy conversion efficiency coefficient (–)
a_{kin}	Kinetic energy conversion efficiency coefficient (–)
c_{p}	Particles' specific heat capacity (J/kg)
d	Measurement volume thickness (mm)
d_{nozzle}	GBK nozzle exit diameter (mm)
DOF	Depth-of-field
E_{j}	Young's modulus of the j-th material (MPa)
FOV	Field-of-view (mm^2)
GBK	Multi-phase flow facility ("Gemischbildungskanal")
G_{p}	Particle mass flux (kg/m^2 s)
Lx	Dimension of VOI in x-axis (mm)
Ly	Dimension of VOI in y-axis (mm)
n_{p}	All particles within VOI at a specific time (#)
p_0	Stagnation pressure (MPa)

✉ Dirk Allofs
dirk.allofs@dlr.de

[1] Supersonic and Hypersonic Flow Technologies Department, DLR, Cologne, Germany

Pr	Prandtl number (–)
R	Gas constant (m^2/Ks^2)
T	Stagnation point surface temperature (K)
T_0	Flow stagnation temperature (K)
T_{back}	Temperature at coaxial-thermocouple's back end (K)
T_p	Particle temperature (K)
VOI	Volume of Interest
V_{p*}	Limiting impact velocity (m/s)
X	X-position of VOI (mm)
Y	Y-position of VOI (mm)
γ	Specific heat ratio (–)
Δ	Shock stand-off distance (mm)
$\Delta\dot{q}$	Increase of convective stagnation point heat flux due to the presence of particles (kW/m^2)
Δt	Double-pulse time separation (ns)
θ_t	Difference between stagnation point surface temperature T at time t_i and the initial stagnation point surface temperature at time t_0 (K)
ρck	Coaxial-thermocouple material constant (W^2s/m^2K^2)
ρ_j	Density of the j-th material (kg/m^3)
ρ_p	Particle density (kg/m^3)
σ_p	Particle's elastic limit (MPa)
σ_s	Elastic limit of the probe's material (MPa)

1 Introduction

In the early 70's, stagnation point heat fluxes in dust-laden supersonic and hypersonic flows were measured first to be far in excess of heat fluxes in dust-free flows (Dunbar et al. 1975). This heat flux increase is commonly named 'particle-induced heat flux augmentation' or 'heating augmentation.' A wide range of physical effects were identified to explain heating augmentation, among them were the conversion of kinetic energy of incident particles into thermal energy (Fleener and Watson 1973; Polezhaev et al. 1992), rebounded particles which were crossing the bow shock and generating additional shear layers or ring vortices (Alkhimov et al. 1982; Holden et al. 1976; Kudin et al. 2013; Levin 1993), turbulence increase of the boundary layer (Bakum and Komarova 1971), the change of the bow shock structure by particle accumulations in front of the probe (Kudin et al. 2013), general bow shock disturbances by particles (Dunbar et al. 1975; Fleener and Watson 1973), and a change of surface roughness and erosion (Dunbar et al. 1975; Osipov et al. 2001).

A common approach to describe heating augmentation is the differentiation of conversion of kinetic energy of the particles into thermal energy and the increase of convective heat flux (Polezhaev et al. 1992; Vasilevskii et al. 2002):

$$\dot{q}_\Sigma = \dot{q}_0 + \Delta\dot{q} + \dot{q}_a \tag{2.1}$$

The measurable stagnation point heat flux in a dust-laden flow $\dot{q}_\Sigma$ is the sum of the stagnation point heat flux in a dust-free flow $\dot{q}_0$, the increase of convective heat flux due to the presence of particles $\Delta\dot{q}$, and the direct energy transfer from particles into the probe $\dot{q}_a$.

The direct particle energy transfer during impact consists of two parts: the conversion of kinetic energy into thermal energy and heat conduction due to differences between particle temperature T_p and probe surface temperature T during particle impact:

$$\dot{q}_a = a_{kin} * \left(\dot{e}_{kin\,inc} - \dot{e}_{kin\,reb}\right) + a_{heat} * G_p * c_p * \left(T_p - T\right) \tag{2.2}$$

This formulation assumes that all particles have the same particle temperature during impact. The parameter a_{kin} is the energy conversion efficiency, also called accommodation coefficient or a_{kin} coefficient, describing the "effectiveness" of particle kinetic energy to be converted into probe heat. The values $\dot{e}_{kin\,inc}$ and $\dot{e}_{kin\,reb}$ are the kinetic energy flux of incident and rebounded particles. The factor a_{heat} and G_p are the thermal energy conversion efficiency coefficient and the particle mass flux of incident particles, respectively. The heat capacity of particles is described with the factor c_p.

The formulation of Eq. (2.2) deviates from those given in literature (Golubkina et al. 2011; Vasilevskii and Osiptsov 1999). This is caused by the fact, that those studies assumed uniform particle sizes as well as uniform particle velocities at impact, as it is also done in (Polezhaev et al. 1992). The kinetic energy flux of rebounded particles $\dot{e}_{kin\,reb}$ is commonly neglected (Fleener and Watson 1973; Polezhaev et al. 1992), as well as the heat conduction aspect, namely the second term on the right-hand side of Eq. (2.2) (Fleener and Watson 1973; Kudin et al. 2013; Polezhaev et al. 1992). This can be reasoned by the short collision time of the particles with the probe surface (Molleson and Stasenko 2014; Polezhaev et al. 1992).

The accommodation coefficient a_{kin} depends on the reflection modus between particles and probe surface (Hove and Shih 1977; Levin 1993; Molleson and Stasenko 2017). The reflection can be described as elastic or inelastic/erosive. An elastic reflection is described for example in (Lashkov 1991) and strongly depends on the material properties of the probe and the particle, as well as on the impact velocity and the impact angle related to the surface. If the particle velocity exceeds a certain value at impact, no rebound from the

probe surface occurs and the reflection can be termed erosive; otherwise, it is elastic or partially elastic (Molleson and Stasenko 2017). This critical value is called limiting impact velocity V_{p^*} in the following and is defined in (Molleson and Stasenko 2017; Stasenko 2007):

$$V_{p^*} = \left[\frac{3}{\rho_p} \left(\frac{1}{\sigma_p} + \frac{1}{\sigma_s} \right)^{-1} \right]^{1/2} \tag{2.3}$$

The parameters ρ_p, σ_p and σ_s are the particle density and the elastic limit of the particle and sample material, respectively. It must be noted that V_{p^*} is not equivalent to the so-called 'critical velocity' of cold spray applications, at which particles start to deposit on the probe surface. Although it is stated that there is no critical velocity for brittle materials like ceramics (Schmidt et al. 2009), the authors have made a comparison between both velocities for classification purposes. Taking the formulation given in (Schmidt et al. 2006) into account and assuming identical particle and probe material, V_{p^*} is approx. 2–4 times lower than the critical velocity for several materials.

The authors of (Molleson and Stasenko 2017) have deduced a theoretical model describing the energy flux from particles to the solid for elastic reflection. This model was only based on the experimental data of (Kudin et al. 2013). It includes normal and tangential velocity components of incident, rebounded, and chaotized particles. Chaotized particles are incident particles interacting with rebounded particles. The authors of (Molleson and Stasenko 2017) mentioned that the concentration of chaotized particles is low in flows with initial particle mass concentrations up to 30%. Since in this work only particle concentrations lower than 1% were investigated, it is assumed that chaotized particles are of minor importance in the following analyses. Considering only the normal velocity components and neglecting chaotized particles, the parameter a_{kin} can be modeled with the following equations:

$$a_{kin} = \frac{\dot{q}_{SP}}{\dot{e}_{kin\,inc} - \dot{e}_{kin\,reb}} = \left[1 + \frac{\sigma_s}{\sigma_p} \left(\frac{b_s}{b_p} \right)^3 \right]^{-1} \tag{2.4}$$

with:

$$b_j = \left(\frac{E_j}{\rho_j} \right)^{0.5} \text{ of j} - \text{material} \tag{2.5}$$

The parameters $\dot{q}_{SP}$, E_j and ρ_j are the measured stagnation point heat flux, the Young's modulus and the density of the j-material, respectively. The heat conduction aspect is neglected in Eq. (2.4).

If particles reflect erosively/inelastic, no a_{kin} formulations but distinct values are given in literature. All literature-listed a_{kin} values for both reflection modes, elastic and erosive, are summarized in Table 1.

(Fleener and Watson 1973) provided the largest dataset of the a_{kin} coefficient, containing 20 measured values in the range of 0.5–0.9. They have made heating augmentation tests in a hypersonic Mach number 6.1–9.5 air flow regime and 100–200 µm large SiC and MgO particles. The achieved particle mass concentrations were in the range of 0.001–10% (Dunbar et al. 1974, 1975; Fleener and Watson 1973). The stagnation point heat flux was measured with backface thermocouples. The a_{kin} coefficient was derived from the calculated heat flux at that time at which the probe surface reached the gas stagnation temperature in a dust-laden flow. The authors of (Kudin et al. 2013) measured an a_{kin} coefficient of 0.17 in a Mach number 2.3 combustion gas and nitrogen flow regime and 27–111 µm large SiO2 particles. The particle mass concentration was up to 25%. Both studies approximated the reduction of particle impact velocity in the shock layer and measured a time-averaged particle mass flux to calculate the incident particle kinetic energy flux. A detailed summary of selected experimental studies is given in Table 12 in the Appendix. This selection considers only studies in which explicit heating augmentation data were presented.

There is only a limited number of experimentally determined a_{kin} coefficients for a limited number of materials (see Table 1). Many particle-induced heating augmentation studies, among them (Golubkina et al. 2011; Hove and Shih 1977; Hove and Taylor 1976; Ishii et al. 1990; Levin 1993; Polezhaev et al. 1992), are based only on the results of (Dunbar et al. 1975). An

Table 1 Summary of a_{kin} coefficients from literature

Particle material [–]	Probe material [–]	V_p at impact [m/s]	Reflection modus [–]	a_{kin} [–]	Source [–]	Remarks
SiC/MgO	6AL-4 V titanium alloy	< 884	Elastic	0.7 ± 0.2	(Fleener and Watson 1973)	Reflection modus named in (Hove and Shih 1977)
–	–	–	Erosive	0.3	(Hove and Shih 1977; Levin 1993)	No reference explanation given
SiO_2	Copper	564		0.17	(Kudin et al. 2013)	–
SiO_2	Copper	907	Erosive	0.1	(Molleson and Stasenko 2017)	Data from (Kudin et al. 2013)

extension of experimentally determined a_{kin} coefficients in supersonic dust-laden flows is therefore of high importance. This work presents new experiments concerning the determination of the a_{kin} coefficient. While the heat conduction aspect of Eq. (2–2) is neglected, both particle kinetic energy fluxes, namely $\dot{e}_{kin\,inc}$ and $\dot{e}_{kin\,reb}$, are derived from individual particle sizes and velocities, which are measured with highly resolved shadowgraphy. This spatially and temporally resolved measurement technique was tested and validated in previous investigations (Allofs et al. 2022). It allows analyzing both, incident and rebounding particles. To the best knowledge of the authors, this is the first time that temporally resolved individual particle sizes and velocities are accounted for the analysis of the accommodation coefficient a_{kin}.

The purposes of this work are summarized as follows:

- Measurement of velocity and kinetic energy reduction of individual particles within the shock layer
- Determination of particle reflection mode by considering V_{p^*}
- Check, if the common neglection of the kinetic energy of rebounded particles for a_{kin} coefficient determination is appropriate
- a_{kin} coefficient determination for 20–60 µm sized Al_2O_3, MgO, and SiO_2 particles in a Mach number 2.1 air flow regime
- Comparison of the a_{kin} coefficient formulation by (Molleson and Stasenko 2017) to experiments

2 Methods

2.1 Test facility setup

Tests were performed in the multi-phase flow facility (GBK), which is a blow down facility, using high-pressurized air from reservoir tanks. The maximum design pressure of the GBK facility is 5.4 MPa, while the maximum design temperature is 800 K. Two different air flows can be controlled automatically: A heatable pure air flow, named 'main' flow, and an unheated dust-laden flow, named 'bypass' flow in the following. Particles were seeded with an in-house developed seeding device. A detailed description of the GBK can be found in (Allofs et al. 2022). The GBK measurement section is illustrated in Fig. 1.

The heatable main flow was mixed with the cold two-phase bypass flow in the injection adapter. Behind the injection adapter, a stagnation chamber with a diameter of 70.3 mm and an ideal-contoured Ma = 2.1 de-Laval nozzle with a nozzle exit d_{nozzle} of 30 mm were placed. The nozzle flow was directed into a diffusor, which was located at the end of a test chamber. The flow stagnation temperature T_0 was measured with a 1.1 mm diameter type K thermocouple in front of the nozzle. The stagnation pressure p_0 was

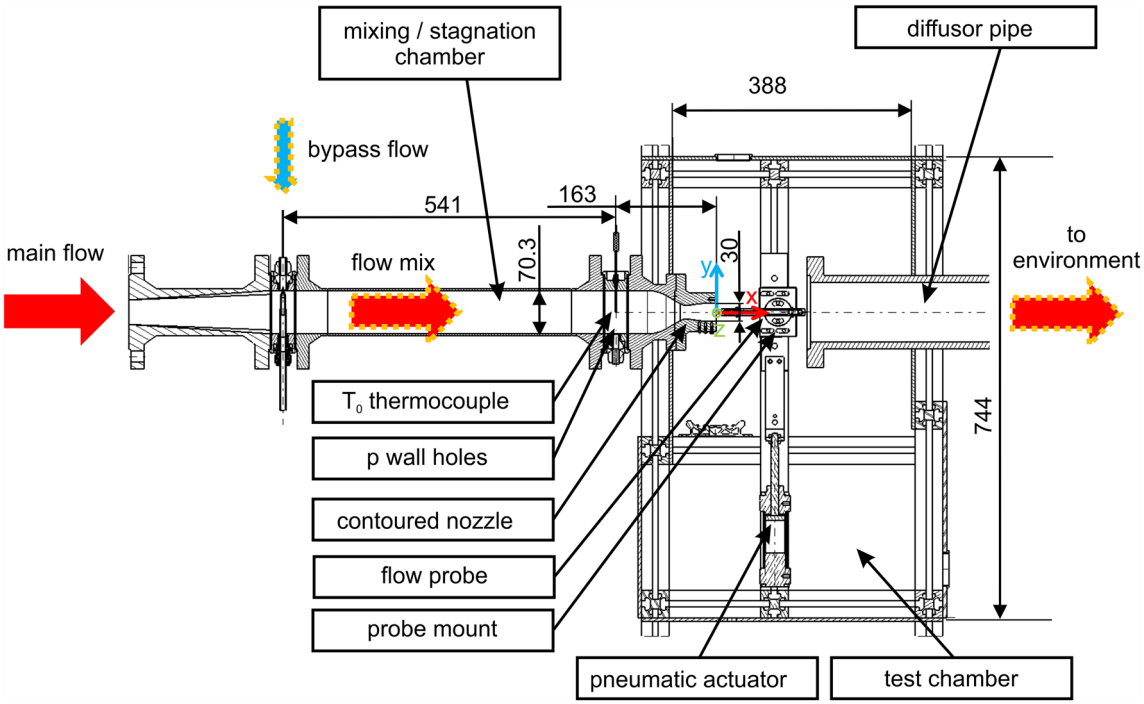

Fig. 1 Sectional side view of the GBK measurement section, dimensions given in mm (adapted from (Allofs et al. 2022))

reconstructed by means of the wall pressure close to the T_0 sensor.

2.2 Shadowgraphy

Particles were analyzed with a highly resolved shadowgraphy system. This system was one of two implemented optical systems, namely PTV and shadowgraphy, whose setup were the same as described in (Allofs et al. 2022). An overview of both optical setups is sketched in Fig. 2. In this study, only data of the shadowgraphy system are considered.

The illumination source was a 'SpitLight DPSS 250 PIV' laser system of InnoLas Laser GmbH, generating two light pulses with a nominal time separation (Δt) of 400 ns at a repetition rate of 100 Hz and a wavelength of 532 nm. The 532 nm laser light was used for the PTV measurements and for feeding the shadow diffusor of Dantec Dynamics GmbH. The shadow diffusor generated a background illumination with a wavelength range of 532 nm to approx. 564 nm. Several wavelength filters were used to separate PTV and shadowgraphy measurements properly. Only light in the wavelength range of 550 nm to approx. 564 nm was used for shadowgraphy measurements by implementing 550 nm long-pass filters behind the shadow diffusor and in front of the shadowgraphy cameras. The 532 nm laser light is marked green and the shadowgraphy background illumination is marked yellow in Fig. 2. The maximum illumination area of the shadow diffusor was 112 mm in diameter. With a set of half-wave plates and beam splitters, the energy for shadowgraphy and PTV illumination was controlled. A maximum pulse energy of 30 mJ was used to feed the shadow diffusor. An additional photodiode was used to control and to correct the pulse time separation Δt. The timing of laser and cameras as well as the camera data acquisition was controlled by a PTU-X timing unit of LaVision and the LaVision DaVis ParticleMaster software V10.1.

The high-magnification shadowgraphy system consisted of two LaVision Imager sCMOS cameras (named C1 and C2 in Fig. 2), having a pixel size of 6.5 µm. A long-distance microscope K2 Distamax of Infinity Photo-Optical Company was equipped with a CF-1b lens, a 'Zoom Module', and an optical beam splitter so that both cameras used the same optics. To avoid double exposure by the 100 Hz laser system, only a central sensor area of 1060×2560 px^2 for C1 and C2 was used, ensuring a double-image rate of 50 Hz for each camera. The cameras were recording one after the other, resulting in a shadowgraphy double-image recording rate of 100 Hz. The optical magnification was increased to 327.5 px/mm by increasing the optical amplification level of the 'Zoom Module.' The aperture control of the long-distance microscope was set to the middle position, resulting in an aperture opening of approx. 17 mm in diameter. C1 and C2 were equipped with 550 nm long-pass filter. The working distance between lens and focus plane was 361 mm. The resulting shadowgraphy field-of-view (FOV) was 3.2×7.8 mm^2. An example of the entire shadowgraphy FOV is given in Fig. 3. Shadowgraphy was capable to see a part of the incident flow, the bow shock, the shock layer, as well as a part of the probe tip. Incident particles were analyzed in an area in front of the shock, called 'freestream' analysis area and marked with a purple rectangle, while rebounded

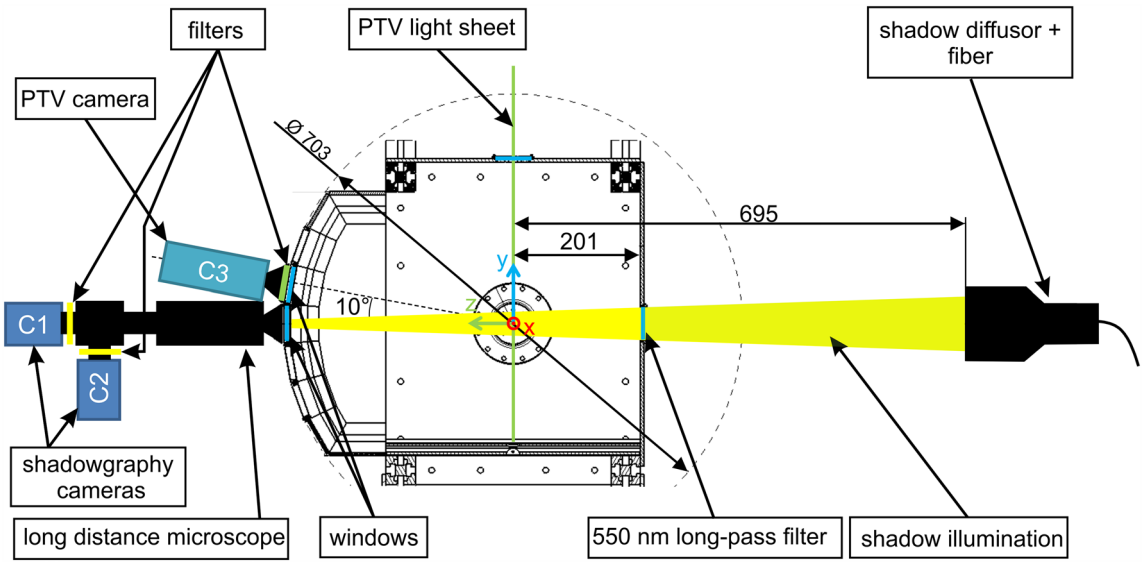

Fig. 2 Front view on the PTV and shadowgraphy setup, dimensions given in mm (adapted from Allofs et al. 2022)

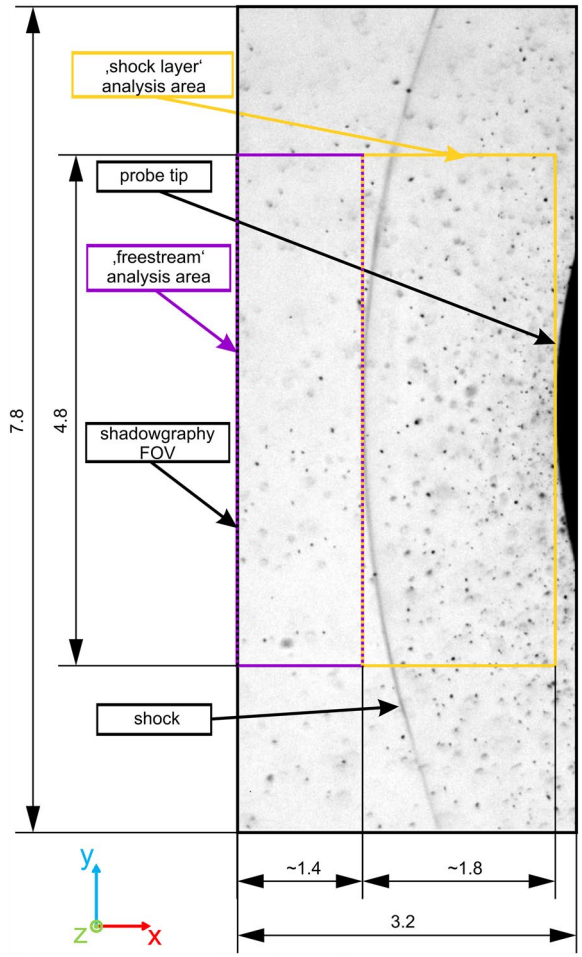

Fig. 3 Sketch of shadowgraphy's FOV: 'freestream' analysis area (purple) in front of the bow shock, while the 'shock layer' analysis area contains the entire shock layer (orange)

particles were analyzed in the shock layer, called 'shock layer' analysis area and marked with an orange rectangle. The distance between shock and probe called the shock stand-off distance (Δ) was measured for each test. On average, the incident particles analysis area was approx. 1.4×4.8 mm^2, while the rebounded particles analysis area was approx. 1.8×4.8 mm^2. The freestream analysis area for the detection of incident particles was kept similar to those described in (Allofs et al. 2022) to comply with the validated results of particle mass flux. The effect of the analysis area selection on the resulting incident particle mass flux and incident particle's kinetic energy is covered in Sect. 3.1.

DaVis ParticleMaster software measured the individual particle velocity with an implemented particle tracking algorithm. Particle shadow displacements were between 40 and 80 px. Particle size and particle mass flux were measured with LaVision DaVis ParticleMaster V10.1 software and an additional particle size and measurement volume correction. The analysis procedure is described in detail in (Allofs et al. 2022). The smallest detectable particle size was 6 µm. The depth-of-field (DOF) was less than 6 mm for particles smaller 60 µm.

Velocity filters were applied to distinguish between incident and rebounded particles. These filters are listed in Table 2 and Table 3, respectively. The freestream gas velocity was calculated with one-dimensional isentropic relations and is named 'theoretical velocity' in the following.

Individual particle characteristics were used to calculate the particle kinetic energy flux $\dot{e}_{\mathrm{kin}}$. Assuming spherical particles and a constant particle density ρ_{p} for all particles, the particle kinetic energy flux was calculated as follows:

$$\dot{e}_{kin}(t,X,Y) = \frac{4}{3} * \pi * \frac{\rho_{\mathrm{p}}}{\mathrm{Lx} * \mathrm{Ly}} * \sum_{i=1}^{n_{\mathrm{p}}(t,X,Y)} \frac{\left(\frac{d_{\mathrm{pi}}}{2}\right)^3 * V_{\mathrm{pi}}^3}{d_i}, \left[\dot{e}_{\mathrm{kin}}\right] = \frac{W}{m^2} \tag{3.1}$$

The Volume-Of-Interest (VOI) has the dimensions Ly and Lx with the thickness d. It is located at the position X and Y. All particles in VOI at time t are summarized with n_{p} (t, X, Y). Shadowgraphy's measurement volume thickness d is a function of the particle diameter d_{p}, and hence, it must be placed within the sigma sign in Eq. (3–1). The parameter V_{p} is the magnitude of the particle velocity.

The particle kinetic energy flux was calculated for each shadowgraphy image. It was additionally smoothed with a rolling-average filter with a length of 25 samples. This filter was used to reduce strong oscillations in particle kinetic energy flux and the resulting a_{kin} coefficient data. Those oscillations were caused by several "empty" shadowgraphy images in which no particles were detected.

The resulting particle size uncertainty for all particle sizes is 1.25 µm (Allofs et al. 2022). The overall particle velocity uncertainty is 0.2 px. It was found that the overall particle

Table 2 Overview of applied filters to detect incident particles

Parameter	Unit	Filter
X-component of particle velocity	m/s	300 to theoretical velocity
Y-component of particle velocity	m/s	−20 to 20

Table 3 Overview of applied filters to detect rebounded particles

Parameter	Unit	Filter
X-component of particle velocity	m/s	−600 to −20
Y-component of particle velocity	m/s	−200 to 200

mass flux measurement uncertainty is 30% and is dominated by particle mass flux variations due to changes in particle detection settings (Allofs et al. 2022). The authors assume that a measurement uncertainty of the same order of magnitude can be applied to the measured particle kinetic energy fluxes.

2.3 Probe installation

The stagnation heat flux was derived from temperature data of a type-E coaxial thermocouple. This thermocouple was manufactured by the Supersonic and Hypersonic Flow Technologies Department of DLR. It had a thread-less 1.9 mm diameter tip and a metric M2.5 thread for mounting. Its total length was 18 mm. The coaxial thermocouple was mounted into a hemispherical-shaped axisymmetric probe head made of stainless steel (1.4539) and fixed with a nut. The probe head was insulated to decrease the coaxial-thermocouple signal noise. The probe head and the insulator were clamped into the head mount with clamping screws. Alignment edges were used for accurate re-positioning of the probe head. The head mount including the probe head and the insulator had a total length of 60 mm. The probe nose diameter d_{Probe} was 12 mm. A sketch of the coaxial-thermocouple installation as well as the probe head is illustrated in Fig. 4. The distance between probe tip and nozzle exit varied between 4 and 6 mm, which was caused by thermal expansion of the nozzle.

The probe head as well as the coaxial thermocouple was polished with a 2000-grit sandpaper before each test run. Subsequently, an activation of the thermocouple was done. The seeded particles slightly eroded the probe head, resulting in a change of the probe head shape from hemispherical to parabolic. The probe head shape was scanned once with a Keyence VR-5000 optical microscope after the tests made with Al_2O_3 and before tests made with SiO_2 and MgO. The probe shape profiles of a vertical ($z=0$ mm) and of a horizontal ($y=0$ mm) plane are depicted in Fig. 5. A hemispherical profile is shown for reference purposes. The probe hat shape change is underlined by the decrease of the shock

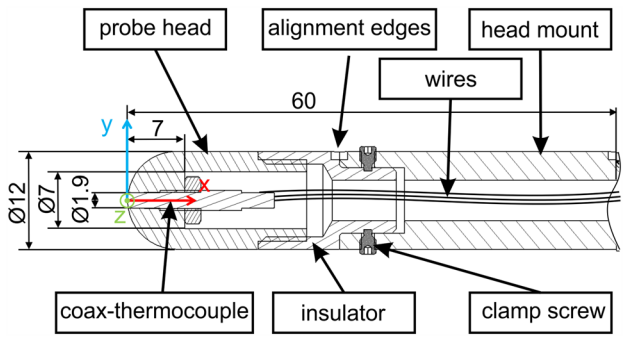

Fig. 4 Sketch of probe setup, dimensions given in mm

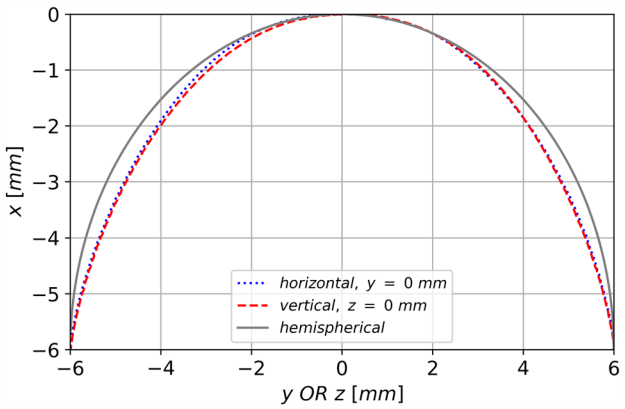

Fig. 5 Probe shape during the test series, horizontal ($y=0$ mm) and vertical ($z=0$ mm) profile

stand-off distance Δ from 1.93 to 1.68 mm during the entire test series (see Table 8, tests are not sorted in chronological order).

The following equations are based on the Cook–Felderman equations (Cook and Felderman 1966) and were used for stagnation point heat flux $\dot{q}_{\mathrm{SP}}$ calculation (like in (Thiele et al. 2018)):

$$\dot{q}_{\mathrm{SP}}(t_{\mathrm{n}}) = \frac{2\sqrt{\rho \mathrm{ck}}}{\sqrt{\pi}} \sum_{i=1}^{\mathrm{n}} \frac{\Theta(t_i) - \Theta(t_{i-1})}{(t_{\mathrm{n}} - t_i)^{0.5} + (t_{\mathrm{n}} - t_{i-1})^{0.5}} \tag{3.2}$$

with:

$$\Theta(t_i) = T(t_i) - T(t_0) \tag{3.3}$$

The factor ρck is the coaxial-thermocouple material constant, and θ_{ti} is the difference between stagnation point surface temperature T at time t_i and the initial stagnation point surface temperature at time t_0.

The Eq. (3.2) is based on the theory of one-dimensional heat conduction into a semi-infinity body with constant material properties. The authors assume that lateral heat fluxes can be neglected in this analysis. The given equation is only valid as long as the temperature at the coaxial thermocouple's back end T_{back} is constant. T_{back} was measured with a second thermocouple placed at the coaxial thermocouple's back end. The authors assumed that Eq. (3.2) can be applied as long as follows:

$$\Theta_{\mathrm{back}}(t_i) = T_{\mathrm{back}}(t_i) - T_{\mathrm{back}}(t_0) < 0.1K \tag{3.4}$$

The thermocouple's raw signals were recorded with 50,000 Hz. In a first step, the raw signal was smoothed with a 500-sample-length rolling-average filter and

Table 4 Particle properties

Particles	Manufacturer	Material name	d_{V10}	d_{V50}	d_{V90}	ρ_p	σ	E
Unit	[–]	[–]	[µm]	[µm]	[µm]	[kg/m^3]	[1e9 Pa]	[1e9 Pa]
Al_2O_3	H.C. Starck GmbH	Amperit 740.065	17.5	27.5	37.5	3884	0.74	320
MgO	Lehmann & Voss & Co. KG	LUVOMAG M-045, sieved	15.0	20.0	30.0	3134	0.125	300
SiO_2	Sigma-Aldrich, Merck SA	83340	20.0	47.5	75.0	2636	0.37	100

Table 5 Probe and coaxial-thermocouple material properties

Probe material	Manufacturer	Material name	ρ	E	σ
Unit	[–]	[–]	[kg/m^3]	[1e9 Pa]	[1e9 Pa]
Stainless steel	Ugine	1.4539	8000	195	0.263
Constantan	Isabellenhütte Heusler GmbH	Isotan	8900	160	0.25
Chromel	Isabellenhütte Heusler GmbH	Isatherm-	8700	180	0.40

down-sampled to the shadowgraphy's recording rate of 100 Hz. This signal was additionally smoothed with a second rolling-average filter with a length of 25 samples to agree with shadowgraphy data smoothing. The resulting temperature signal was used for heat flux computation.

The measurement uncertainty of the heat flux is determined as follows: The material constant uncertainty is assumed to be 5%. The measurement uncertainty for each of the down-sampled temperature signal was assumed to be the standard deviation of all considered 500 temperature samples. The heat flux measurement uncertainty was calculated by applying linear error propagation theory.

2.4 Particles and material constants

Three different particle materials were used for seeding, namely alumina (Al_2O_3), magnesium oxide (MgO) and silica (SiO_2). Volume-based diameters are given in Table 4 for a rough size characterization. As an example, 90% of the entire particle volume is cumulated on all particles smaller than d_{V90}; 10% of the entire particle volume is cumulated on all particles smaller than d_{V10}. The shown values are taken from shadowgraphy measurements at the reference flow condition (see Sect. 2.5). Additional detailed particle size distributions can be found in (Allofs et al. 2022). A pycnometer was used to measure particle density ρ_p. While Al_2O_3 and SiO_2 densities were close to values from literature, MgO density was determined to be significantly smaller. This was explained by a partial chemical reaction of MgO with humidity to $Mg(OH)_2$, which has a density of 2380 kg/m^3 (Allofs et al. 2022). Considering the measured particle density of 3134 kg/m^3, the nominal MgO material could be a MgO/$Mg(OH)_2$ mix with a mass mixing ratio of 63% MgO–37% $Mg(OH)_2$. Since MgO is dominating, the authors assume that the mechanical properties of that mix can be approximated with those of MgO. Furthermore, this material is named 'MgO' in the following. The parameter σ is the Yield strength or the elastic limit of the material and were taken from (Molleson and Stasenko 2017) and (Azom 2023). Table 4 lists all relevant particle properties. Characteristic probe and coaxial-thermocouple material properties are summarized in Table 5. These values were required for the modelling processes.

Table 6 V_{p^*} for all particle/probe material combinations

V_{p^*} [m/s]	Al_2O_3	MgO	SiO_2
Stainless steel	387	285	418
Constantan	380	282	412
Chromel	**448**	**302**	**468**

Table 7 General flow constants

Parameter	Unit	Value
Flow		
γ	–	1.4
R	m^2/(s^2 K)	287.058
c	m^2/s^2 K	1004.798
Pr	–	0.71
Ma	–	2.1

The limiting impact velocity V_{p^*} is calculated with Eq. (2.3) and summarized for each particle/probe material combination in Table 6. Material properties of chromel were taken into consideration for following analyses, because the

major cross section of the coaxial-thermocouple is made of it and because lateral heat conduction from the stainless-steel probe head into the coaxial-thermocouple is neglected in the formulation given in Eq. (3.2). The resulting V_{p^*}, calculated with chromel material properties, is plotted in Sect. 3.1 and is marked bold in Table 6.

2.5 Test conditions

A total of 16 tests were performed. While the nozzle contour and the resulting Mach number remained constant, T_0, p_0, and particle material were varied. The Reynolds number Re_{dProbe}, based on the probe nose diameter d_{Probe} and freestream conditions, ranged from 6e5 to 1.8e6. Specific flow properties are assumed to be constant, namely the gas constant R, the specific heat ratio γ, the specific heat capacity c, as well as the Mach number and the Prandtl number Pr. Their values can be found in Table 7.

An overview of all tests is given in Table 8. Tests are sorted by particle material, T_0, and p_0. The temporal mean of the particle mass concentration is expressed by c_m. The reference flow condition was $T_0 = 373$ K and $p_0 = 0.96$ MPa. Four different p_0 levels, namely 1:0.6 MPa, 2:0.96 MPa, 3:1.3 MPa, and 4:1.7 MPa, and three different T_0 levels, namely 1:303 K, 2:338 K, and 3:373 K, were tested with Al_2O_3 particles. For the other materials, only the variation in p_0 was performed. For each run, a synonym was defined in the form: material–temperature level/pressure level. For example, the synonym 'A-32' stands for the run with Al_2O_3 particles, on the third temperature level of 373 K, on the second pressure level of 0.96 MPa. The active seeding time was set to 10 s. Table 8 also lists the air mass flow $\dot{m}_{air}$, the Reynolds number based on the probe nose diameter d_{Probe}, and the shock stand-off distance Δ.

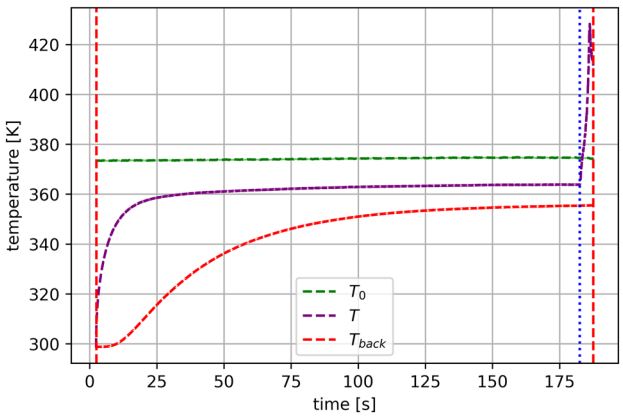

Fig. 6 Time curves of the coaxial-thermocouple (purple: front, red: back) and the stagnation temperature T_0 of test run A-32. The measurement period is in between the two vertical red dashed lines. The particle injection started at $t = 180$ s, marked with a blue dotted line

The injection time of the probe was set to 185 s. The idea was to heat the probe in a dust-free flow up to a quasi-stationary temperature level, so that convective heating effects can be excluded. This procedure is similar to those described in (Dunbar et al. 1974, 1975; Fleener and Watson 1973). The probe was heated up in a dust-free flow for 180 s, which was sufficient to achieve a constant temperature at the thermocouple's back end. The particle injection was activated for 10 s, and the probe was removed from the flow 5 s after the particle injection start.

Table 8 Test matrix, sorted by particle material, T_0, and p_0

Synonym [–]	p_0 [MPa]	T_0 [K]	$\dot{m}_{air}$ [g/s]	Re_{dProbe} [–]	Δ [mm]	c_m [%]
A-11	0.594	303.3	529.8	8.13E+05	1.88	0.700
A-12	0.958	303.7	847.2	1.31E+06	1.93	0.293
A-13	1.288	303.5	1152.0	1.76E+06	1.88	0.363
A-14	1.686	303.9	1507.9	2.30E+06	1.86	0.178
A-22	0.950	338.4	803.4	1.12E+06	1.77	0.837
A-31	0.593	373.8	476.1	6.10E+05	1.81	0.094
A-32	0.951	374.2	765.2	9.77E+05	1.80	0.639
A-33	1.286	373.2	1032.9	1.33E+06	1.78	0.042
A-34	1.682	373.3	1354.7	1.73E+06	1.81	0.191
M-31	0.594	373.6	476.6	6.11E+05	1.69	0.242
M-32	0.949	373.5	764.1	9.78E+05	1.70	0.218
M-33	1.289	373.5	1036.7	1.33E+06	1.71	0.096
M-34	1.684	373.7	1355.4	1.73E+06	1.68	0.115
S-31	0.592	373.9	476.3	6.09E+05	1.70	0.776
S-32	0.951	373.7	764.4	9.79E+05	1.70	0.514
S-33	1.288	373.6	1034.9	1.33E+06	1.70	0.057

The time curves of the probe's temperatures are given in Fig. 6 for the reference flow condition. The measurement period is in between the two red dashed lines. The particle injection started at $t = 180$ s, marked with a blue dotted line. The particles' impact increased the measured stagnation point surface temperature T. The authors assumed that the application of the Cook–Felderman method (Cook and Felderman 1966) (see Eq. (3.2)) is valid for the period of particle injection. This was reasoned by constant temperatures at both ends of the coaxial-thermocouple prior particle injection. As a consequence, the resulting stagnation point heat flux corresponds only to the direct energy transfer from particles into the probe $\dot{q}_a$. It was observed that a lower quasi-stationary surface temperature at the stagnation point T was measured, compared to the stagnation temperature T_0. The measured quasi-stationary surface temperature at the stagnation point T is in fair agreement to the recovery temperature.

3 Results

3.1 Energy flux of incident particles

Particles are generally decelerated when passing the shock layer. The effect of particle deceleration on the resulting kinetic energy flux of all incident particles at reference flow condition for three particle materials is illustrated in Figs. 7, 8, and 9. The orange error bars represent the velocity IQR of all particles in the freestream ('fs', see Sect. 2.2), while the blue error bars represent the velocity IQR of all particles in the shock layer ('sl'). The red dotted lines represent the limiting impact velocity V_{p*} (see Table 6). The

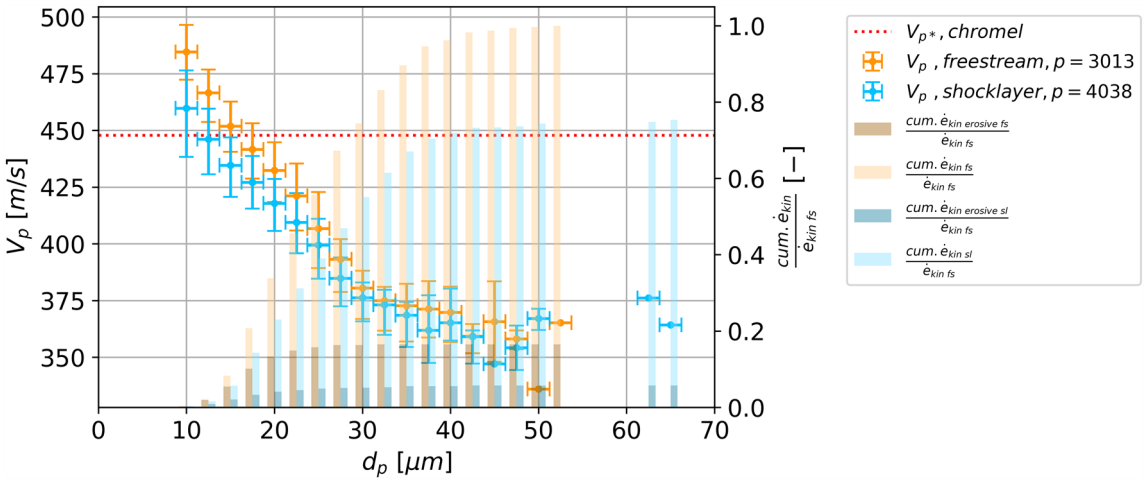

Fig. 7 Relation between particle velocity, size, and the kinetic energy of incident particles in the freestream and in the shock layer, run ID A-32

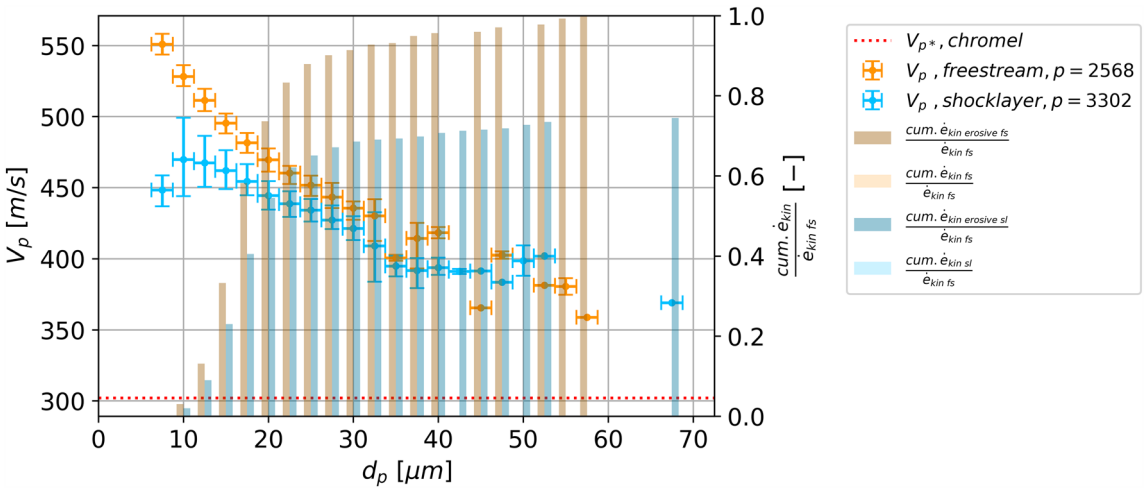

Fig. 8 Relation between particle velocity, size, and the kinetic energy of incident particles in the freestream and in the shock layer, run ID M-32

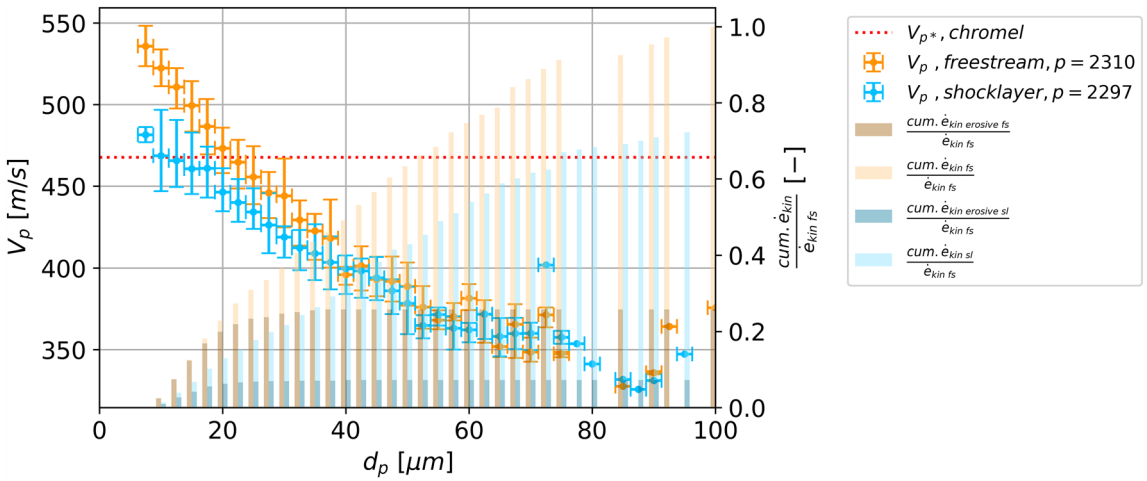

Fig. 9 Relation between particle velocity, size, and the kinetic energy of incident particles in the freestream and in the shock layer, run ID S-32

total numbers of all considered particles are given in the figure legends.

The kinetic energy flux of incident particles with sizes up to the given value on the x-axis is called 'cumulated' kinetic energy flux (cum.$\dot{e}_{kin}$) in the following. The parameter cum.$\dot{e}_{kin}$ is considered for both analysis areas, the freestream and the shock layer. Both of the cumulated kinetic energy fluxes are scaled to $\dot{e}_{kin\ fs}$, the kinetic energy flux of all incident particles in the freestream. These ratios are shown as light bars. As an example, approximately 50% of the kinetic energy flux in the freestream is distributed on particles smaller than 22.5 µm (Al_2O_3), 17.5 µm (MgO), or 40 µm (SiO_2) (light orange bars). The darker parts of the bars represent the ratio of the cumulated erosive kinetic energy flux cum.$\dot{e}_{kin\ erosive}$ and $\dot{e}_{kin\ fs}$. The cumulated erosive kinetic energy flux considers only particles faster than V_{p*} (see Sect. 2.4).

The absolute velocity difference of particles in the freestream and in the shock layer increases with decreasing particle size. The velocity IQR range of particles in the shock layer is larger compared to those of particles in the freestream, especially for smaller particle sizes. This is caused by the continuous deceleration of particles in the shock layer and the summation of particles just entering the shock layer and particles already traveling through the shock layer.

The kinetic energy flux of incident particles in the shock layer is approx. 8–29% smaller than those of particles in the freestream. The detected percentage of the erosive kinetic energy flux is reduced significantly for Al_2O_3 and SiO_2 particles in the shock layer. These energy flux reductions are mainly caused by the particle deceleration. An overview of detected kinetic energy flux reduction in the shock layer is given in Table 9.

Table 9 Kinetic energy flux reduction due to particle deceleration within the shock layer

Synonym [–]	Re_{dProbe} [–]	$\frac{\dot{e}_{kin\ inc\ erosive\ fs}}{\dot{e}_{kin\ inc\ fs}}$ [%]	$\frac{\dot{e}_{kin\ inc\ erosive\ sl}}{\dot{e}_{kin\ inc\ sl}}$ [%]	$\frac{\dot{e}_{kin\ inc\ sl}}{\dot{e}_{kin\ inc\ fs}}$ [%]
A-11	8.13E+05	0	0	76
A-12	1.31E+06	1	0	77
A-13	1.76E+06	7	1	73
A-14	2.30E+06	19	1	71
A-22	1.12E+06	6	3	74
A-31	6.10E+05	3	1	92
A-32	9.77E+05	16	7	75
A-33	1.33E+06	36	14	87
A-34	1.73E+06	66	29	79
M-31	6.11E+05	100	100	82
M-32	9.78E+05	100	100	74
M-33	1.33E+06	100	100	82
M-34	1.73E+06	100	99	72
S-31	6.09E+05	8	5	82
S-32	9.79E+05	25	9	72
S-33	1.33E+06	27	11	83

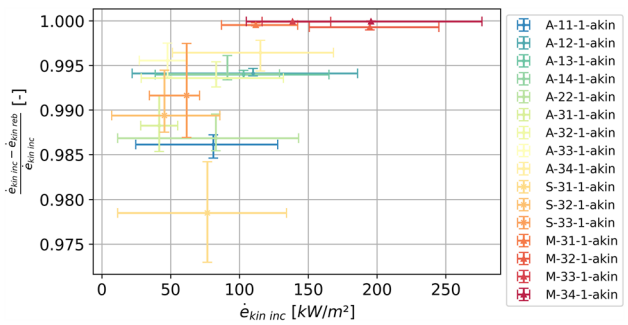

Fig. 10 Significance of rebounded particle kinetic energy flux, compared to incident particle kinetic energy flux for all tests

Table 10 Estimated a_{kin} coefficient for all particle/probe material combinations. The right term of Eq. (2.4) was used for computation

a_{kin} [–]	Al_2O_3	MgO	SiO_2
Stainless steel	0.95	0.79	0.73
Constantan	0.97	0.86	0.82
Chromel	**0.94**	**0.76**	**0.70**

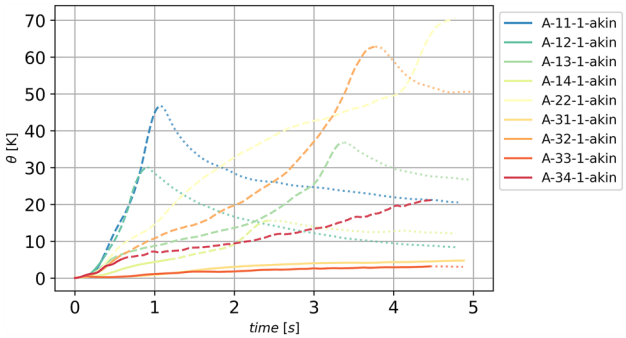

Fig. 11 Temporal change of θ for all tests with Al_2O_3 particles

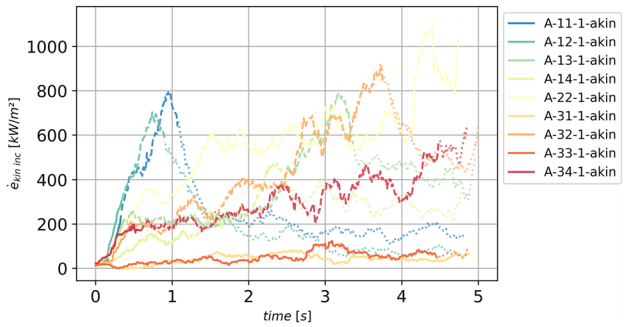

Fig. 12 Temporal change of $\dot{e}_{kin\ inc}$ for all tests with Al_2O_3 particles

The distribution of kinetic energy flux on different particle sizes is a complex function depending on particle size, particle material, and flow conditions (see Figs. 7, 8, and 9)). The kinetic energy of incident particles in the shock layer $\dot{e}_{kin\ inc\ sl}$ is considered in following analyses.

3.2 Energy flux of rebounded particles

The scaled difference between incident particle kinetic energy flux $\dot{e}_{kin\ inc}$ and rebounded particle kinetic energy flux $\dot{e}_{kin\ reb}$ is compared in Fig. 10 to estimate the influence of the rebounded particle kinetic energy flux on the determination of the a_{kin} coefficient (see Eq. (2.4)). The bars indicate the

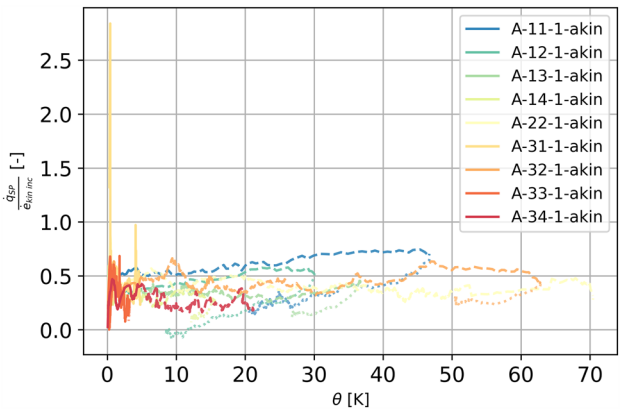

Fig. 13 a_{kin} Coefficient versus relative stagnation point temperature θ

mean and the interquartile range (IQR) of each test. The scaled difference of the kinetic energies $\dot{e}_{kin\ reb}$ and $\dot{e}_{kin\ inc}$ is slightly increasing with increasing $\dot{e}_{kin\ inc}$ for Al_2O_3 and SiO_2 tests, but it is less than 2.5%. Almost no rebounded MgO particle was detected. The authors assume that the neglection of the kinetic energy flux of rebounded particles $\dot{e}_{kin\ reb}$ is reasonable for the following analysis.

3.3 a_{kin} Coefficient

The a_{kin} coefficient is estimated with the formulation in Eq. (2.4) to compare with experimental results. This formulation is only valid for elastic particle reflection, meaning that the percentage of erosive kinetic energy flux is zero. Calculated values are given in Table 10. The influence of the selected probe material on the estimated a_{kin} coefficient is not significant.

The temporal changes of the measured relative stagnation point surface temperature θ as well as $\dot{e}_{kin\ inc}$ are plotted in Figs. 11 and 12, respectively. Data of all tests with Al_2O_3 particles were considered for these plots. The time on the x-axis is set to 0 at the start of the particle injection, which is approx. 180 s after probe injection (see Fig. 6). Significant unexpected variations of the $\dot{e}_{kin\ inc}$ were observed. While for most of the tests $\dot{e}_{kin\ inc}$ is increasing with time, some tests show maximum $\dot{e}_{kin\ inc}$ right after seeding start with a decrease with increasing time. The relative stagnation point surface temperature behaves similar to $\dot{e}_{kin\ inc}$. Data before the maximum achieved stagnation point surface temperature are marked with a solid and a dashed line; the data beyond this point are marked with a dotted line. The difference between the solid line and a dashed line is explained below.

Considering the results of Sect. 3.2 and neglecting the heat conduction aspect, the a_{kin} coefficient is determined experimentally with the following equation:

$$a_{kin} = \frac{\dot{q}_{SP}}{\dot{e}_{kin\ inc} - \dot{e}_{kin\ reb}} \sim \frac{\dot{q}_{SP}}{\dot{e}_{kin\ inc}} \tag{4.1}$$

This ratio of all Al_2O_3 tests is shown in Fig. 13. Like in Figs. 11 and 12, data before the maximum achieved stagnation point surface temperature are marked with a solid and a dashed line, the data beyond this point are marked with a dotted line. The a_{kin} coefficient is decreasing when the maximum stagnation point surface temperature is reached. Furthermore, it becomes smaller than zero when the stagnation point surface temperature is decreasing for a longer time period (see A-12). The larger the temperature difference θ, the larger the potential impact of convection effects. To minimize the effect of convection cooling on the determination of the a_{kin} coefficient, only data are considered in which θ is smaller than 5 K. These data are marked in Figs. 11, 12, and 13 with a solid line. Peaks of the a_{kin} coefficient larger than unity can be explained by short time periods, in which only few particles were detected. Figure 13 does not contain measurement uncertainties for better visibility of the measured mean values.

The ratio of erosive kinetic energy flux $\dot{e}_{kin\ inc\ erosive}$ and the kinetic energy flux of all incident particles $\dot{e}_{kin\ inc}$ was considered to distinguish between an elastic and an erosive particle reflection environment. Material properties of chromel were taken into consideration for the calculation of V_{p*}. If stainless steel is considered as probe material, V_{p*} is

Table 11 Measured a_{kin} coefficients

Synonym	Re_{dProbe}	$\frac{\dot{e}_{kin\ inc\ erosive\ sl}}{\dot{e}_{kin\ inc\ sl}}$	a_{kin}	IQR a_{kin}
[–]	[–]	[%]	[–]	[–]
A-11	8.13E+05	0	0.42±0.02	0.33–0.51
A-12	1.31E+06	0	0.32±0.02	0.29–0.35
A-13	1.76E+06	1	0.34±0.02	0.30–0.38
A-14	2.30E+06	1	0.32±0.01	0.28–0.35
A-22	1.12E+06	3	0.50±0.02	0.41–0.56
A-31	6.10E+05	1	0.44±0.01	0.31–0.46
A-32	9.77E+05	7	0.44±0.02	0.39–0.48
A-33	1.33E+06	14	0.26±0.00	0.16–0.33
A-34	1.73E+06	29	0.33±0.01	0.26–0.40
M-31	6.11E+05	100	0.12±0.00	0.11–0.16
M-32	9.78E+05	100	0.09±0.00	0.08–0.10
M-33	1.33E+06	100	0.08±0.00	0.06–0.09
M-34	1.73E+06	99	0.06±0.00	0.05–0.07
S-31	6.09E+05	5	0.36±0.02	0.26–0.45
S-32	9.79E+05	10	0.85±0.05	0.52–1.10
S-33	1.33E+06	11	0.36±0.01	0.17–0.43

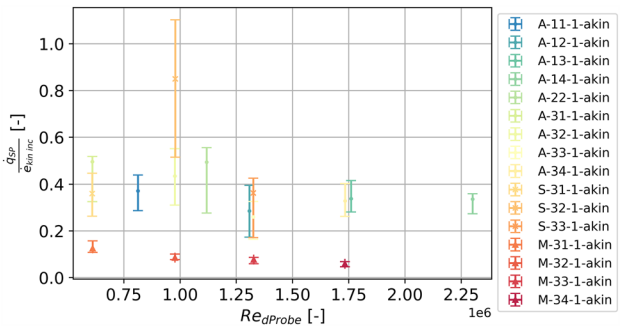

Fig. 14 Measured a_{kin} coefficient versus Re_{dProbe} for all tests

reduced and hence, the percentages of erosive kinetic energy flux would increase.

The measured a_{kin} coefficients of all tests are summarized in Table 11. The experimentally determined a_{kin} coefficient is in the range of 0.26–0.50, 0.36–0.85, and 0.06–0.12 for Al_2O_3, SiO_2, and MgO particles, respectively. The respective mean values are 0.37, 0.52, and 0.09. All MgO particle tests provided a complete erosive particle reflection environment. Generally, it seems that the determined a_{kin} coefficient of test run S-32 has an outlier character. If this outlier is excluded, the determined mean a_{kin} coefficient of SiO_2 particle tests is 0.36, very close to those of Al_2O_3 particle tests.

The measurement uncertainty of the mean a_{kin} coefficient as well as the IQR of the considered temporally resolved a_{kin} coefficients for each test is also listed in Table 11. The mean a_{kin} coefficient values as well as the measurement uncertainty were rounded to two decimal figures. The estimated measurement uncertainties are smaller than the temporal a_{kin} coefficient variations, which are shown in Fig. 13 and which are considered in the IQR.

Since there is a link between particle-induced heating augmentation and Re_{dProbe} (Fleener and Watson 1973), this study analyzed the dependency of the a_{kin} coefficient on Re_{dProbe} and plotted it in Fig. 14. A monotonically decreasing a_{kin} coefficient was observed only in tests with MgO particles. The IQR bars of the a_{kin} coefficient of Al_2O_3 tests are too large for an appropriate relation interpretation.

4 Discussion

The implementation of highly resolved shadowgraphy measurements allowed to quantify the degree of kinetic energy reduction of particles passing a bow shock. Test data showed that the kinetic energy flux of incident particles is reduced by approx. 8–29% due to the deceleration of particles within

the shock layer. The distribution of the kinetic energy flux on different particle sizes depends on the particle size distribution and the flow condition. In this context, the consideration of individual particle characteristics for kinetic energy flux determination within the shock layer seems to be essential.

The kinetic energy flux of rebounded particles within the entire shock layer is less than 2.5% of the incident particle kinetic energy flux. Hence, the kinetic energy flux of rebounded particles was neglected for the measurement of the a_{kin} coefficient in this study. Since almost no rebounded MgO particles were found, the question arises whether these particles broke up during impact into pieces which are smaller than 6 µm (the resolution limit of the implemented shadowgraphy system) or whether they stuck on the probe surface. Future investigations of the probe surface could give answers to this. Generally, a larger kinetic energy flux of rebounded particles would increase the a_{kin} coefficient, if the formulation of Eq. (2.4) is considered.

The a_{kin} coefficient is assumed to be the ratio between measured heat flux and kinetic energy flux of incident particles in the shock layer. The time curves of the temperature and kinetic energy flux indicate that the particle seeding was not homogeneous during these tests. It seems that the uncertainty of determination of the a_{kin} coefficient itself depends on the temporal change of the kinetic energy flux of incident particles. It is shown that convective cooling phases of the probe reduced the a_{kin} coefficient significantly, even to negative values. On the one hand, extending the range of considered θ would possibly smooth the measured a_{kin} coefficient by increasing the number of data points, but on the other hand, potential convection cooling effects become stronger. Therefore, limiting the θ range of up to 5 K seems to be a good trade-off to exclude convection cooling effects from the author's point of view, although even within this small temperature difference range some cooling phases were observed. Future studies should focus on the improvement of homogeneous particle seeding, since a temporal-homogeneous seeding should simplify the data analysis.

The experimentally determined a_{kin} coefficients are between 0.26 to 0.50, 0.36 to 0.85, and 0.06 to 0.12 for Al_2O_3, SiO_2, and MgO particles, respectively. The respective means are 0.37, 0.36, and 0.09, respectively, considering one outlier exclusion for the SiO2 tests. The a_{kin} coefficients determined for Al_2O_3 and SiO_2 particles are in good agreement to the erosive a_{kin} coefficient value of 0.3, mentioned in the study of (Hove and Shih 1977). Moreover, the experimentally determined MgO a_{kin} coefficient of 0.09 is in good agreement with the suggestion of (Molleson and Stasenko 2017) for the a_{kin} coefficient in erosive environments.

The decrease of the MgO-based a_{kin} coefficient with increasing Re_{dProbe} can be explained with stronger cooling or ablation effects in erosive environments. Previous particle-induced heating augmentation studies state a decrease of the a_{kin} coefficient from elastic to erosive environments. This behavior cannot be reproduced with the experiments presented in this study, based on the characterization of the particle reflection behavior with V_{p^*} (Stasenko 2007). If stainless-steel material properties were considered in the calculation of V_{p^*}, instead of chromel properties, V_{p^*} would decrease and hence, the percentage of erosive incident particle kinetic energy flux would be higher.

The a_{kin} coefficient for elastic particle reflection, suggested by (Molleson and Stasenko 2017), was simplified and compared to experimental data. It seems that the simplified formulation overestimates the a_{kin} coefficient by a factor of approx. 2 for Al_2O_3 and SiO_2 particles. This might be caused by a higher $\dot{e}_{kin}$ detection rate of shadowgraphy, compared to the measurement techniques used in (Kudin et al. 2013). The difference of up to 29% of the kinetic energy flux of particles in the shock layer and in the freestream seems to be too small to be an explanation. Because MgO tests were completely erosive, a direct comparison is not feasible.

5 Conclusion

The key findings of this work can be summarized as follows:

- The deceleration of incident particles in the shock layer reduced the kinetic energy flux of incident particles up to 29%, depending on particle material and flow conditions.
- the measured kinetic energy flux of rebounded particles in the entire shock layer was less than 2.5% of the kinetic energy flux of incident particles.
- The experimentally determined a_{kin} coefficient is approx. 0.36 for Al_2O_3 and SiO_2 particles, while it is approx. 0.09 for MgO particles. No difference between erosive and elastic particle reflection mode was detected on the a_{kin} coefficient.
- The a_{kin} coefficient decreases with increasing Re_{dProbe} for MgO particles.

Appendix

Overview of selected experimental particle-induced heating augmentation analyses

See Table 12.

Table 12 Experimental setups for supersonic two-phase flows

Parameter	Unit	Fleener and Watson	Dunbar et al	Polezhaev et al	Vasilevski and Osiptsov	Kudin et al
Year		1973	1975	1992	1999	2013
Flow parameters						
Facility		Arc heater, AEDC/DETF, BHWT	Arc heater, AEDC/DETF, BHWT	Liquid fuel combustion chamber, gas dynamic tube	TsAGI UT-1, short-duration	TsAGI GGUM, liquid fuel combustion chamber
Gas	–	Air	Air	Combustion gas	Air, CO_2, N_2	Combustion gas, N_2
Ma_∞	–	6.1—9.5	6.1—9.5	2.6—4.2	6	2.26, 2.39
$Re_{1\infty}$	1/m	4.43e6—6.18e7	4.43e6—6.18e7	5e6—12.5e7		
$H_{0\infty}$	kJ/kg	279—4187	279—4187	3700		
$T_{0\infty}$	K				570	290—1600
$p_{0\infty}$	MPa	0.02—0.203	0.02—0.203	20	0.21—3.3	1.5
Probe parameters						
Probe shape	–	Hemisphere, disk	Hemisphere, disk	Hemisphere, disk	Hemisphere, disk	Hemisphere, disk
Probe nose radius R_N	mm	6.35, 12.7, 30.2, 38.1	12.7, 25.4, 38.1	20, 40	3, 6, 12, 24	8.1, 16.2, 25.65
Probe diameter d_{Probe}	mm	12.7, 25.4, 60.4, 76.2	25.4, 50.8, 76.2	40, 80	6, 12, 24, 48	16.2, 32.4, 51. 3
Probe material	–	6Al-4 V titanium alloy	Titanium, Inconel, stainless steel, platinum, graphite	Copper	Aluminum	M3 grade copper, copper
Particle parameters						
Particle material	–	MgO, SiC	MgO, SiC, glass	Al_2O_3	Si_3N_4, SiO_2, Fe_2O_3, Cr_2O_3, Fe	SiO_2
Nominal d_p	10e-6 m	100, 200	100, 200, 650	20, 100, 250	0.12, 0.15, 0.27, 0.75, 2.4, 161	27—111
Particle shape					Approx. spherical, except CrO_3 and Fe_2O_3	Irregular
Material preparation					Dried at 450 K, wrapped in metal foil	–
c_m	%	0.001—10	0.001—10	0.1—1	1-25	0—25
$V_{p\infty}$	m/s	762—1707	762—1707		1000	564, 907
$V_{p\ imp}$	m/s			1000—1500		
General information						
Heat flux measurement	–	Back face thermocouples, thin skin heat transfer model	Back face thermocouple, thin skin heat transfer model	Thin wall copper calorimeter with chromel—copper thermocouple	Thin wall calorimeter, stainless steel foil band, grounded	Calorimeter
Particle characterization techniques		Analytic ($V_{p\infty}$)	Double pulsed holography	Analytic ($V_{p\ impact}$)	Philips SEM-515 scanning electron microscope, two wavelength intensity ratio (dp), analytic ($V_{p\infty}$)	Electron microscope, particle storage receiver, kind of LDA
Particle concentration measurement		Analytically + dust catcher calibration	Analytically + dust catcher calibration	Analytically + recording membranes	Analytically + scattered light registration	Optical light attenuation, particle storage receiver

Table 12 (continued)

Parameter	Unit	Fleener and Watson	Dunbar et al	Polezhaev et al	Vasilevski and Osiptsov	Kudin et al
Flow visualization techniques	–	1000 Hz Schlieren system	Shadowgraph	–	Shadow method	Shadow method, pressure sensor
Investigation focus	–	Rebounded particle-induced turbulence	Fundamental heat augmentation analysis	Influence of probe size/shape, particle concentration and size, flow pressure and non-equilibrium factors	Influence of small particle sizes	Fundamental heat augmentation analysis
Remarks	–	Some data identical to Dunbar et al., additional tests with different Re Number	Some data identical to Fleener and Watson		Noticed electrical disturbances, data averaged from 4 – 20 ms; tests repeated 3—6 times	

Acknowledgements The authors would like to thank you the mechanical team of Supersonic and Hypersonic Technologies Department, especially Daniel Jäger, for their mechanical and manufacturing support and Christian Hantz for his linguistic revision.

Author contributions DA contribution to this work includes conceptualization, methodology, formal analysis, and investigation, original draft preparation as well as editing. DN contributed review, and technical expertise to this work. AG contributed review, funding acquisition, resources, and supervision to this work.

Funding Open Access funding enabled and organized by Projekt DEAL. This work was fully funded by the DLR's Program Directorate for Space Research and Development in the frame of space transportation research activities.

Data availability For PTV, and shadowgraphy image acquisition, DaVis 10.1.055537 from LaVision GmbH, Anna-Vandenhoeck-Ring 19, 37,081 Goettingen, Germany, was used. For additional data processing, a custom code written in Python 3.8 was used, including common packages as well as: *Uncertainties: A Python package for calculations with uncertainties*, Eric O. LEBIGOT, http://pythonhosted.org/uncertainties/, visited on 21.07.2021. Pco-tools, 1.0.0, https://pypi.org/project/pco-tools/#files, visited on 21.07.2021. ReadIM, 0.84., https://pypi.org/project/ReadIM/, visited on 21.07.2021. Lvreader, v1.2.0, https://www.lavision.de/en/downloads/software/python_add_ons.php, visited on 30.07.2022.

Declarations

Conflict of interest The authors have no relevant financial or non-financial interests to disclose.

Ethical approval Not applicable.

Consent for publication No special consent required for publication.

Consent to participate No special consent required for participation.

References

Alkhimov AP, Nesterovich NI, Papyrin AN (1982) Experimental investigation of supersonic two-phase flow over bodies. J Appl Mech Tech Phys 23:219–226. https://doi.org/10.1007/BF00911002

Allofs D, Neeb D, Gülhan A (2022) Particle mass flow determination in dust-laden supersonic flows by means of simultaneous application of optical measurement techniques. Exp Fluids. https://doi.org/10.1007/s00348-022-03567-7

Bakum BI, Komarova GS (1971) The effect of dust in the working stream of hypersonic wind tunnels on the results of heat-transfer measurements. J Eng Phys 21:1361–1363. https://doi.org/10.1007/BF01271345

Cook WJ, Felderman EJ (1966) Reduction of data from thin-film heat-transfer gages—a concise numerical technique. AIAA J 4:561–562. https://doi.org/10.2514/3.3486

Dunbar LE, Courtney JF, Mcmillen LD (1975) Heating augmentation in erosive hypersonic environments. AIAA J 13:908–912. https://doi.org/10.2514/3.60468

Dunbar L, Courtney J, Mcmillen L (1974) Heating augmentation in particle erosion environments 8th aerodynamic testing conference

Fleener W, Watson R (1973) Convective heating in dust-laden hypersonic flows 8th thermophysics conference.

Vasilevskii E, Osiptsov A (1999) Experimental and numerical study of heat transfer on a blunt body in dusty hypersonic flow 33rd thermophysics conference. American institute of aeronautics and astronautics

Thiele T, Gülhan A, Olivier H (2018) Instrumentation and aerothermal postflight analysis of the rocket technology flight experiment rotex-T. J Spacecr Rockets 55(5):1050–1073

Allofs D, Neeb D, Gülhan A (2022) Simultaneous Determination of Particle Size, Velocity, and Mass Flow in Dust-Laden Supersonic Flows. Exp Fluids. https://doi.org/10.1007/s00348-022-03402-z

Azom (2023) Mgo Material Properties. Azom, https://www.azom.com/properties.aspx?ArticleID=54, pp. MgO material properties

Golubkina IV, Osiptsov AN, Sakharov VI (2011) Supersonic low-concentration dusty-gas flow past a plane cylinder in the presence of an oblique shock wave interacting with the bow shock. Fluid Dyn 46:51–63. https://doi.org/10.1134/S0015462811010066

Holden M, Duryea G, Gustafson G, Hudack L (1976) An experimental study of particle-induced convective heating augmentation 9th fluid and plasmadynamics conference.

Hove D, Shih W (1977) Reentry vehicle stagnation region heat transfer in particle environments 15th aerospace sciences meeting.

Hove DT, Taylor E (1976) Stagnation region heat transfer in hypersonic particle environments. AIAA J 14:1486–1488. https://doi.org/10.2514/3.7240

Ishii R, Hatta N, Umeda Y, Yuhi M (1990) Supersonic gas-particle two-phase flow around a sphere. J Fluid Mech 221:453–483. https://doi.org/10.1017/S0022112090003639

Kudin OK, Nesterov YN, Tokarev OD, Flaksman YS (2013) Experimental investigations of a high-temperature dust-laden gas jet impinging on an obstacle. TsAGI Sci J 44:869–884. https://doi.org/10.1615/TsAGISciJ.2014011135

Lashkov VA (1991) Experimental determination of the coefficients of restitution of particles in the flow of a gas suspension in a collision against the surface. J Eng Phys 60:154–159. https://doi.org/10.1007/BF00873057

Levin AL (1993) Heat exchange near the critical point of a body within a supersonic two-phase jet. J Appl Mech Tech Phys 34:694–700. https://doi.org/10.1007/BF00859837

Molleson GV, Stasenko AL (2014) Kinetic-thermal effect of a gas-dispersed supersonic jet on an axisymmetric body. High Temp 52:881–889. https://doi.org/10.1134/S0018151X14050125

Molleson GV, Stasenko AL (2017) Gas-dispersed jet flow around a solid in a wide range of stagnation parameters. High Temp 55:87–94. https://doi.org/10.1134/S0018151X1701014X

Osipov MI, Gladoshchuk KA, Arbekov AN (2001) Heat transfer processes in high-temperature flows of two-phase media. Heat Transf Res 32:402–708. https://doi.org/10.1615/HeatTransRes.v32.i7-8.90

Polezhaev YV, Repin IV, Mikhatulin DS (1992) Heat transfer in a heterogeneous supersonic flow. High Temp 30:1147–1153

Schmidt T, Assadi H, Gärtner F et al (2009) From particle acceleration to impact and bonding in cold spraying. J Therm Spray Technol 18:794–808. https://doi.org/10.1007/s11666-009-9357-7

Schmidt T, Gärtner F, Assadi H, Kreye H (2006) Development of a generalized parameter window for cold spray deposition. Acta Mater 54:729–742. https://doi.org/10.1016/j.actamat.2005.10.005

Stasenko AL (2007) Velocity recovery factors of a particle repelled from a solid surface. J Eng Phys Thermophys 80:885–891. https://doi.org/10.1007/s10891-007-0119-4

Vasilevskii E, Dombrovsky LA, Mikhatulin DS, Polezhaev YV (2002) Heat transfer in a heterogeneous supersonic flow. Heat transfer, proceedings of the 12th international heat transfer conference 12